Monte Carlo Simulations and Atomic Calculations for Auger Processes in Biomedical Nanotheranostics†

Maximiliano Montenegro,‡ Sultana N. Nahar,*,‡ Anil K. Pradhan,*,‡,§ Ke Huang,|| and Yan Yu||

Department of Astronomy, The Ohio State University, Columbus, Ohio 43210, Chemical Physics Program, The Ohio State University, Columbus, Ohio 43210, and Jefferson Medical College, Thomas Jefferson University, Philadelphia, Pennsylvania 19107

Received: June 5, 2009; Revised Manuscript Received: July 31, 2009

We present numerical simulations of X-ray emission and absorption in a biological environment for which we have modified the general-purpose computer code Geant4. The underlying mechanism rests on the use of heavy nanoparticles delivered to specific sites, such as cancerous tumors, and treated with monoenergetic X-rays at resonant atomic and molecular transitions. X-ray irradiation of high-*Z* atoms results in Auger decays of photon emission and electron ejections creating multiple electron vacancies. These vacancies may be filled either be radiative decays from higher electronic shells or by excitations from the K-shell at resonant energies by an external X-ray source, as described in an accompanying paper by Pradhan et al. in this volume. Our Monte Carlo models assume normal body material embedded with a layer of gold nanoparticles. The simulation results presented in this paper demonstrate that resonant excitations via Kα, Kβ, etc., transitions result in a considerable enhancement in localized X-ray energy deposition at the layer with gold nanoparticles, compared with nonresonant processes and energies. The present results could be applicable to *in vivo* therapy and diagnostics (theranostics) of cancerous tumors using high-*Z* nanoparticles and monochromatic X-ray sources according to the resonant theranostics (RT) methodology.

Introduction

The normal body tissue is primarily composed of light elements, mainly H, C, N, and O, and their molecular compounds. As such, the interaction of X-rays with most of the matter at atomic and molecular scales is weak. In spite of the wide use of X-rays in imaging and therapy, the overall usage is inefficient and reflected in unnecessary exposure to large radiation dosage. This is because the X-ray sources in medical facilities produce broadband bremsstrahlung radiation spanning a wide energy range up to the highest voltage in the X-ray tube. A large part of this radiation is not used for any treatment. Consequently, low-energy X-rays are absorbed by the intervening healthy tissue up to the site under investigation, while high-energy X-rays pass through without much interaction.

Enhancing the efficiency of X-ray utilization in medicine for therapy and diagnostics (theranostics) is of obvious interest for practical applications. In an accompanying paper in this volume, Pradhan et al.[1] have outlined a scheme termed "Resonant Theranostics" (RT) based on the use of monochromatic X-ray sources, high-*Z* elements, and nanobiotechnology.[2] It is well-known that the (i) total interaction cross sections of X-rays increase with atomic number *Z* and (ii) absorption/emission of high-energy X-rays up to nearly 100 keV may be exploited for biomedical applications by using high-*Z* elements toward the upper end of the periodic table. Noble elements such as platinum and gold afford the advantages in both of these factors, since they correspond to $Z = 78$ and 79, respectively, as well as the fact that they are mostly nonreactive and nontoxic for medical purposes. The use of high-energy X-rays coupled with high-*Z* elements offers another great advantage: they penetrate more deeply into the body tissue, thereby enabling imaging diagnostics and therapeutic pathways for *in vivo* treatment of, for example, cancerous tumors.

However, at present, the technical infrastructure needed to implement the RT methodology[2] is not yet available. While different aspects of the methodology—availability of monochromatic X-ray sources and manufacture, targeting, and delivery of nanoparticles to tumor sites—are under development, it is desirable to study the underlying physical processes theoretically and computationally. Moreover, it is highly instructive to carry out numerical simulations, such as using Monte Carlo models, of the pathways that would be required and implemented by the RT methodology. The resonant Auger effect has been discussed extensively in the literature, as also explained in the accompanying paper by Pradhan et al.[1] In addition, simulations of atomic and molecular dynamics and the Auger effect have been addressed for special cases in heavy elements,[3] and the water molecule.[4] For example, the former study[3] focuses on the behavior of resonances and the Raman Auger spectrum in the vicinity of ionization thresholds for several neutral atoms such as Mg, Ar, Kr, Xe, etc., and the importance of electron correlation effects is investigated. The study on the water molecule (Takahashi et al., 2006), simulates the core−hole excited-state molecular dynamics and compares with experiments. It is found that the computed Auger spectrum of the water molecule is insensitive to the dynamics, but the ultrafast dissociation due to oxygen $1s \rightarrow 4a_1$ transition is very sensitive to initial vibrational distortions in the ground state. Whereas these studies serve to elucidate important aspects of the Auger processes and dynamics, at the present time, they are prohibitively computationally intensive in complex simulations involving heavy elements and compounds in different environments.

† Part of the "Russell M. Pitzer Festschrift".

* E-mail: nahar@astronomy.ohio-state.edu (S.N.N.); pradhan@astronomy.ohio-state.edu (A.K.P.).
‡ Department of Astronomy, The Ohio State University.
§ Chemical Physics Program, The Ohio State University.
|| Thomas Jefferson University.

10.1021/jp905323y CCC: $40.75
Published on Web 08/27/2009

Numerical simulations, using the available atomic data for rates, can shed light on the overall picture by using the Monte Carlo scheme widely used for modeling a variety of complex situations, including biophysical environments. Geant4 includes the Auger process via an extension referred to as the low-energy electromagnetic process, as discussed later. It is this package that has been modified in this work to consider resonant enhancement and fluorescent yields that may be utilized for monochromatic imaging and diagnostics, as well as therapy.

X-ray Induced Processes and Radiative Transitions

In this paper, we seek to model the physical processes due to irradiation of X-rays and passage through body tissue interspersed with layers of high-Z material. The aim is to study the enhanced X-ray interactions owing to the presence of high-Z material, and at resonant energies as opposed to the nonresonant background. The radiosensitizing agents commonly used in medicine are composed of molecules such as bromodeoxyuridine (BUdR) or iodeoxyuridine (IUdR) that contain atoms of heavy elements. Increasingly, the application of nanobiotechnology entails nanoparticles made of high-Z elements such as platinum and gold, in targeted antigens. The background X-ray absorption cross sections are large for heavier elements for ionization of outer electronic shells. However, they are small for inner-shell electrons which are likely to be ionized at high X-ray energies needed for deep penetration into the body tissue.

Most of the basic theoretical calculations of RT methodology depend on the atomic physics of high-Z atoms which is poorly known. Since X-ray interaction with high-Z atoms implies inner-shell ionization, absorption, and emission, the associated Auger processes of photon and electron emission play a dominant role. An Auger process is dropping of an electron in a higher level to an electron vacancy in a lower or inner shell. The characteristic of this process is that a photon of energy equal to the difference of the two levels is emitted which in turn can knock out another electron of the higher level, creating two vacancies in the higher level. Hence, the emission of a photon and an electron are assoicated with the Auger process. The filling up lower vacancies can result in a cascade of electrons and photons. While most of the relevant rates for all of these Auger processes for heavy elements have not yet been computed, in a previous study, we have computed radiative transition probabilities for resonant transitions in gold ions.[5] In the present paper, we employ a general-purpose Monte Carlo code Geant4,[7] making use of atomic calculations reported in the earlier paper by Nahar et al.[5] As discussed by Pradhan et al.[1] in this volume, it is known that Auger processes induced by ionization of the innermost K-shell in heavy elements, comprising radiosensitizing agents such as BUdR, are not sufficiently strong. They do not lead to significant enhancement in emission of electrons and photons for breakup of DNA that might support the use of high-Z material.

Previous studies have relied on X-ray absorption through ionization of K-shell electrons at energies of the K-shell ionization threshold and just above it where the cross sections shows a rise over the background. We showed in the accompanying Pradhan et al.[1] paper the presence of high peak resonances in absorption cross sections which are orders of magnitude higher than that for K-shell ionization. In this paper, we invoke the RT mechanism activated via these resonances below the K-shell ionization threshold, particularly at energies for Kα (1s−2p) transitions. It is assumed that K-shell ionization can lead to vacancies in higher electronic shells due to Auger cascade as high-level electrons drop to fill in the lower level vacancies. Thus, an incident monoenergetic Kα beam of X-rays with sufficient intensity may be able to do the inverse process to excite the K-shell electrons into the L-shell (and also into higher shells through resonant transitions of Kβ (1s−3p), Kγ (1s−4p), etc.).

Theoretical modeling using the Monte Carlo method of Auger processes induced by monoenergetic X-ray beams requires mainly the photoionization or photoelectric cross sections and radiative transition probabilities for the core transitions in high-Z atoms (as obtained earlier for gold[5]).

Monte Carlo Simulations for X-ray Absorption

Modeling of photon transport in biological tissue numerically with Monte Carlo simulations is common, as it can provide accurate enough predictions compared to handling a difficult radiation transfer equation or diffusion theory. Monte Carlo simulations can keep track of multiple physical quantities simultaneously, with any desired spatial and temporal resolution making it a powerful tool. The simulations can be made arbitrarily accurate by increasing the number of photons traced. Hence, the methods are often considered the standard for simulated measurements of photon transport for many biomedical applications. Although flexible, Monte Carlo modeling is rigorous, since it is statistical and therefore requires significant computation time to achieve precision. In this method, transportation of photons is expressed by probability distributions which describe the step size of photon propagation between sites of photon−tissue interaction and the angles of deflection in the photon's trajectory when a scattering event occurs. The required parameters needed are the absorption coefficient, the scattering coefficient, the scattering phase function, etc. As the photon interacts with the medium, it deposits energies due to absorption and is scattered to other parts of the medium. Any number of variables can be incorporated along the way, depending on the interest of a particular application. Each photon packet will repeatedly undergo the following numbered steps until it is either terminated, reflected, or transmitted (for Monte Carlo discussion, see, for example, ref 6).

The simulation of radiation effects in biological systems is critical in various domains, such as oncological radiotherapy and radiation protection. In these fields, the irradiation of a biological system is usually described in terms of the overall radiation dose deposited. However, that measure is inadequate to describe the effect of radiation in microscopical entities, such as cellular structures and the DNA molecule. A more useful description comes from microdosimetry or nanodosimetry,[8] that accounts for the energy deposition of particles over track lengths of the order of a few nanometers or tens of nanometers, compatible with the DNA size. However, few general Monte Carlo codes have the capability of describing particle interactions at these scales. In general, standard Monte Carlo codes, like EGS,[9] Fluka,[10] and MCNP,[11] approach collisions as binary processes, where target electrons are treated as free and at rest, or the influence of electronic binding is accounted for in an approximate way. Moreover, their calculation of dose distributions is based on particle transport, valid only if the binding energies are small compared with discrete energy loss events. This assumption limits the applicability of these codes to particle energies greater than 1 keV. On the other hand, more specialized Monte Carlo codes, known as "track structure codes"[12] have been developed for microdosimetry calculations for radiobiological studies, like the evaluation of molecular damage. The main differences among them are the media simulated, the phenomenological or theoretical model used, and the experi-

mental data implemented. Most of the microdosimetry Monte Carlo simulations have been carried out with these codes and only for radionuclides.[13] Unfortunately, all of these codes are not open source, nor publicly distributed as software libraries or executables.

An exception to these rules is the general Monte Carlo code Geant4[7] and its package extension known as low-energy electromagnetic processes.[14] Geant4 is an open source code developed with an object-oriented design that provides the possibility to implement or modify any physical process in Geant4 without changing other parts of the code. This feature makes Geant4 open to extensions of its physics modeling capabilities and to the implementation of alternative physics models. Initially designed to deal with high-energy physics experiments, its versatility has enabled application to broader domains, from instrumentation[15] to medical physics.[16] The Geant4 low-energy electromagnetic package is the product of a wider project called Geant4-DNA, which addresses specifically the extension of Geant4 to simulate radiation effects at the cellular and DNA scale, and has been widely tested.[17]

However, this Geant4 package still treats atoms as neutral, and photoelectric cross sections do not include electronic shell-ionization effects. The standard version of Geant4 we have modified to accomorate resonant structures does not include the shell structures in an atomic system and hence is incapable of treating the Auger cascade process. The main modification we have made in the Geant4 package is to include resonant excitation cross sections for contributing ionization stages of a specific high-Z element, in the present instance gold ($Z = 79$). The purpose is to compare total X-ray absorption efficiency due to resonant Kα excitation as opposed to that due to background ionization in the standard version of Geant4.

Phantom Set-Up

We adopted the Monte Carlo code Geant4 version 9.2 for the simulations of X-ray absorption by gold nanoparticles. The photoelectric effect model present in the Geant4 Standard Electromagnetic Process package was modified so that our calculated resonant cross sections could be added to standard values at the resonant energies. We assumed preionization of gold atoms by another X-ray beam at an energy above the K-edge energy of ~81 keV to create electron vacancies, as discussed by Pradhan et al. (2009).[1] The simulations considered resonances for the preionized atomic core of gold ions Au LXXI (or F-like with one electron vacancy) and Au LXXII (or O-like with two electron vacancies). We assume equipartition between these two ion cores. This assumption simplified the calculation of the resonant cross sections and reduced them to be just the average cross sections of both ions, e.g., an estimate of ~2.5 Megabarns (1 MB = 10^{-18} cm^2) at ~68 keV (see previous article of Pradhan et al.[1] in this volume). Outside the resonant energies of these ions, the gold nanoparticles were assumed neutral.

Figure 1 shows the experimental configuration used in our simulations. The dimensions of the phantom were 15 cm × 5 cm × 5 cm, and it was filled with water, as its density is close to that of biological tissues. A region at a depth of 10 cm and dimensions of 2 cm × 5 cm × 5 cm represents a tumor. Simulations were carried out with the tumor region as a water solution of gold nanoparticles at different concentrations by weight. The selection of the concentrations ranging from 0 to 50 mg/mL was based on previous studies that used iodinated contrast agents to enhance dose.[18−22] The phantom was divided longitudinally in sections of 1 mm, and energy deposition as well particle generation at each slice was recorded. A monochromatic linear beam, with a circular cross section of 3 mm in diameter, was aimed at the phantom perpendicular to the square face far from the tumor region (at the left side of Figure 1). Each simulation had 500 000 events, a value that generates error fluctuations of less than 0.1%.

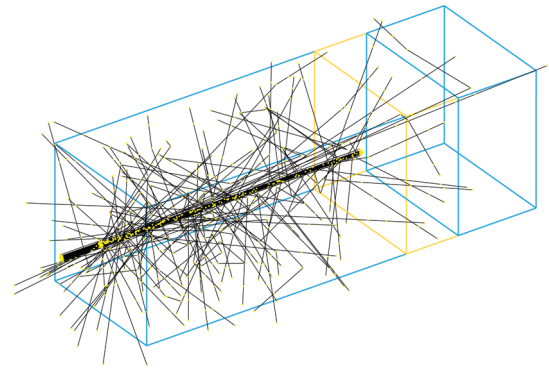

Figure 1. Geometry of the Geant4 simulations. The phantom models a tumor (golden section) 10 cm inside normal tissue (blue section). The monochromatic beam collides perpendicular to the square face far from the tumor region. Black lines show the photon trajectories, and the yellow dots indicate where photons' interactions took place. In this picture, the tumor was embedded with gold nanoparticles at 5 mg/mL and the energy beam was the resonant energy, ~68 keV. Note how only a few photons are able to cross the region before reaching the gold nanoparticles.

In this work, we consider monoenergetic X-ray beams at three different energies corresponding to the atomic structure of the gold atom. The first energy is the averaged Kα (1s−2p transition) energy at 68 keV, which is the energy difference between the L ($n = 2$) and the K ($n = 1$) shell. The second energy is 82 keV, just above the ionization energy of the K-shell electrons at 81 keV. The third energy is a very high energy of 2 MeV, which corresponds to the maximum intensity of the bremsstrahlung radiation distribution from a linear accelerator with 6 MVp peak voltage X-ray source used in many medical facilities. The highest radiation intensity is at about $^1/_3$ of the peak voltage of an X-ray generating tube in an accelerator.

Results and Discussion

One main objective of Monte Carlo simulations is to observe our predicted enhancement in absorption of X-rays at 68 keV resonant energy by the gold nanoparticles, as this will provide a new insight to the unsuccessful experimental searches to find such enhancement at and around the K-shell ionization energy of ~81 keV. Monte Carlo simulation results for X-ray absorption are presented in Figure 2 which shows the mean energy deposited per photon with a depth of the three X-ray beams at energies considered in this study: 68 keV, subsuming the resonant fine structure components Kα1,α2, 82 keV for maximum background K-shell ionization cross section, and 2 MeV corresponding to the maximum intensity of a linear accelerator.

The region between 100 and 120 mm represents the tumor. The top panel shows a simulation with gold nanoparticles embedded in the tumor and irradiated with resonant Kα X-rays at 68 keV, the middle panel corresponds to irradiation by 82 keV, and the bottom panel corresponds to 2 MeV. The rise at the entrance of the tumor in each panel shows the energy deposited at the phantom with gold nanoparticles at a concentration of 5 mg/mL in the tumor. Comparing the two peaks in the top and middle panels, the resonant energy deposition is considerably higher (10.4 for 68 keV compared to 0.2 for 82

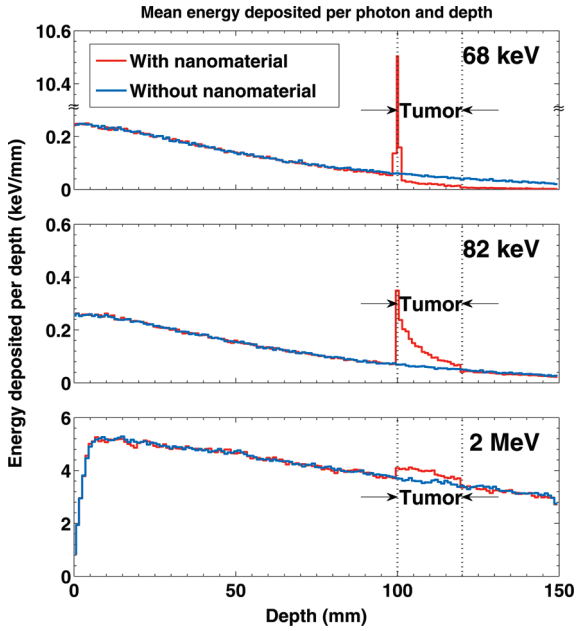

Figure 2. X-ray energy deposited by depth across the phantom for the three X-ray beams used: 68 keV (averaged Kα resonant energy), 82 keV (K-edge energy), and 2 MeV (high energy common in clinical usage). The region between 100 and 120 mm represents the tumor, and it can be embedded with gold nanoparticles at 5 mg/mL (red curve) or water (blue curve). The presence of gold nanoparticles has increased the energy deposited at the tumor, the highest absorption, by more than 25 times that at 82 keV, is at the resonant energy 68 keV (top panel).

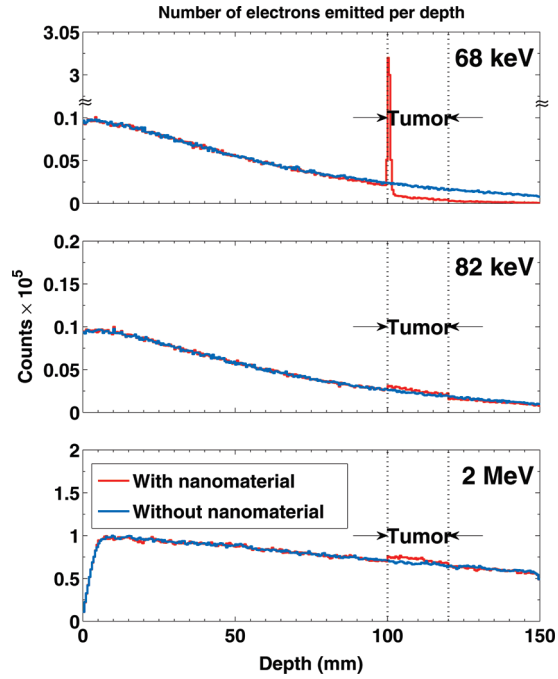

Figure 3. Number of electrons produced with depth for the three X-ray beams at energies of 68 keV, 82 keV, and 2 MeV. A considerably large number of electrons, by much more than an order of magnitude, were produced by 68 keV X-rays compared to those by 82 keV and 2 MeV X-rays.

keV) than the nonresonant value, indicating most of the 68 keV X-rays are absorbed within a millimeter or so of the tumor region due to large resonant cross sections. The enhanced absorption is expectecd to lead to enhanced emission of photons and electrons to kill the tumor cells. The panels show that both the 68 and 82 keV X-ray beams could retain only about quarter of their intensity before reaching the tumor. In fact, there are strong photon interactions, being deflected or absorbed, reducing drastically the number of available photons to interact at the tumor or beyond. On the other hand, the high-energy X-ray beam at 2 MeV in the bottom panel has little interaction with the tissue, and the deposited energy is reduced by only about 20% before reaching the tumor. There is an increase in the energy deposited in the tumor when nanoparticles are present. However, the large amount of energy available per photon of 2 MeV, more than 20 times that of an 82 keV photon, compensates for the low interaction, and the *total* amount of energy deposited is larger than the lower energy beam 82 keV. This is the primary reason why high-energy beams are used in medicinal physics, to ensure that the tumor receives a sufficiently high radiation dose. However, the downside of this approach is that not only the tumor but also the normal tissue along the beam path receive high dosage, as is evident from the bottom panel of Figure 2.

Production of Electrons and Photons. We have studied the production of electrons and photons following the absorption of X-rays by the gold nanoparticles at the three energies. Since these energies, 68 keV, 82 keV, and 2 MeV, are high for any resonance for the water molecules, these molecules experience only Compton scatterings with small cross sections and produce some low-energy electrons. However, the cross section for photoionization or photoelectric effect of the nanoparticles is much more significant in these energies, and considerably large at 68 keV.

Figure 3 presents production of electrons by the medium with water only (blue curve) and water with a thin film of nanoparticles (red curve) at 10 cm from the surface. While a small rise in electron production is noted for 82 keV and 2 MeV (middle and lower panels), a high peak in the electron counts is seen at a resonant energy of 68 keV. A large number of electrons, by more than an order of magnitude, were produced at 68 keV compared to that at 82 keV, an effect that correlates the large energy absorption. Consistent with its larger number of photons reaching the tumor, the high-energy beam at 2 MeV produced more electrons than that at 82 keV, but smaller than that at 68 keV. Actually, the introduction of nanoparticles has a marginal effect for the 2 MeV beam, since the photoelectric cross sections, even for high-Z atoms such as gold, are as low as for the background tissue material made of low-Z elements.

As mentioned, the photoelectrons produced by the X-ray energies are supposed to trigger DNA strand-breaking, and consequently destruction of cancerous cells. The photoelectrons produced in the tumor are absorbed in the immediate vicinity. The mean free paths of electrons produced from gold nanoparticles are 47, 46, and 52 μm for the 68 keV, 82 keV, and 2 MeV beams, respectively, compared with the 1 mm mean free path for photoelectrons produced in the water portion of the phantom.

As expected from details given in the accompanying paper by Pradhan et al.[1] in this volume, most of the input energy from the incident X-ray beams goes into the production of Auger electrons. In contrast to the number of ejected Auger photoelectrons, the counts of *photon* production are marginal, about 3 orders of magnitude lower, as shown in Figure 4 (c.f. the counts on the vertical axis in Figure 3) as a function of depth into the phantom. However, compared to 82 keV and 2 MeV X-ray beams, a surge in photon production by the gold nanoparticles can by seen in the 68 keV curve.

Radiation Dose Enhancement Factor. The radiation dose enhancement is quantified by means of the dose enhancement

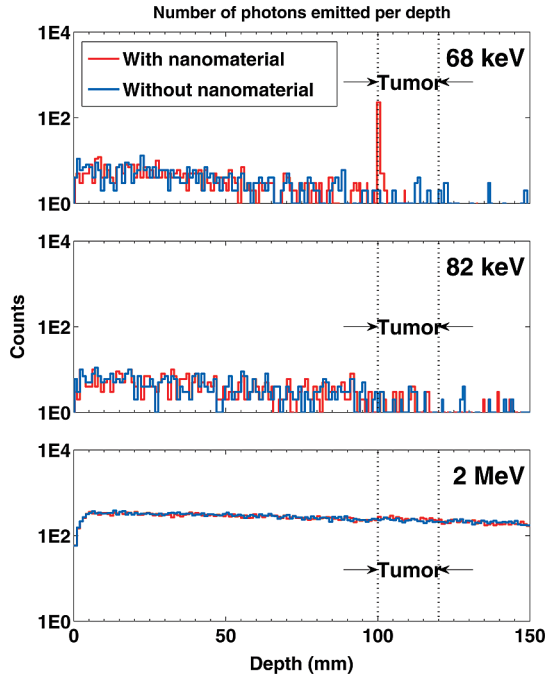

Figure 4. Photon emission with depth for the three X-ray beams. While 82 keV and 2 MeV plots are showing almost no enhancement in photon production by the nanoparticles in the tumor region, a surge of photon production can be seen for the 68 keV curve.

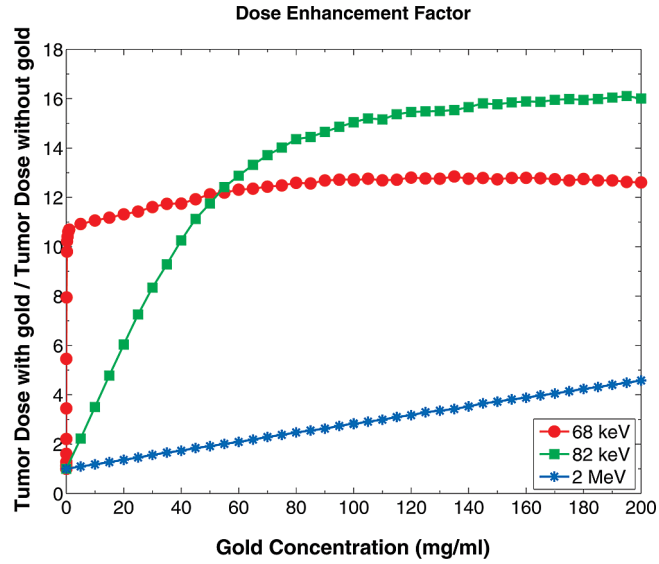

Figure 5. Dose enhancement factors (DEFs) for different concentrations and three energy beams: 68 keV, 82 keV, and 2 MeV.

factors (DEFs).[22] The DEFs are defined as the ratio of the average radiation dose absorbed by the tumor when it is loaded with a contrast medium or agent (viz. iodine) to the dose absorbed without that agent. We will consider the nanoparticle solution as our contrasting medium. From Figure 2, we can obtain by integration the energy absorbed by the tumor with and without nanoparticles. Because we used the same phantom under both conditions, the ratio of the mean total energy absorbed per photon by the tumor under the two conditions is the DEF.

We ran several simulations, varying the gold nanoparticle concentration from 0 to 50 mg/mL. DEFs were obtained by irradiating with the previous three energies: 68 keV, 82 keV, and 2 MeV. The results are plotted in Figure 5. The DEFs obtained for the resonant X-ray beam of 68 keV are 1 order of magnitude greater than those calculated at higher energies using iodine as a contrast agent. At a concentration of 5 mg/mL, the DEF obtained was 11.02, and it increased slowly to 11.7 for a concentration of 50 mg/mL with 68 keV. On the other hand, the DEFs for the beam of 82 keV increased steadily from about 1 to approach the high DEFs obtained in the resonant case. For the 2 MeV case, we obtain low and slowly increasing values of DEFs as the concentration increases, confirming our observation in previous figures: although it is possible to obtain an enhanced dosage with high-energy beams, this enhancement is quite small and it increases very slowly with nanoparticle concentrations. The behavior of the curves is in agreement with the calculations done by Solberg et al.[19] where they obtained that the 250 keV beam had smaller DEFs and a weaker concentration dependence than the 140 keV beam.

The almost flat behavior for the 68 keV DEFs can be explained by the large mass attenuation factor obtained, 39.1 cm^2/g for 68 keV versus 0.241 cm^2/g for 82 keV at 5 mg/mL. This high mass attenuation coefficient produces a complete absorption of any incoming photon to the tumor region within its surface, reducing the transmission probability of a photon and its subsequent absorption beyond. This saturation of the absorption is also observed at high gold concentrations for the 82 keV beam, asymptotically reaching the same value for the 68 keV beam (extension of the results in Figure 5 to higher, though unrealistic, concentrations).

Conclusion

In this work, we report Monte Carlo calculations with the multipurpose code Geant4. The biomedical target consists of a phantom with (i) a region embedded with gold nanoparticles, (ii) at different concentrations, and (iii) irradiated with monochromatic X-ray beams of 68 keV, 82 keV, and 2 MeV. The embedded region represents a tumor at a given depth in normal tissue. The modeling shows that irradiation of X-ray energies result in an enhancement of the radiation dose received by the tumor due to the presence of gold nanoparticles. However, the beam at the resonant energy of 68 keV has the highest absorption and dose enhancement factor, especially at low concentrations that are likely to be used in practical medical applications.

The present simulations illustrate the importance of tuning the energy beam to resonant absorption by the target used, so as to maximize the productions of low-energy Auger electrons that can destroy the malignant cells via DNA strand-breaking. Although high-energy beams have small attenuation and therefore can penetrate deep tumors, they also depose a considerable amount of energy in the normal tissue. The use of high-Z nanoparticles such as gold also constrains the deposited energy locally to the tumor region to reduce the damage in normal tissue. Our study finds that the energy deposition in the tumor can be increased by injecting high-Z nanoparticles, but the enhancement converges at higher concentration. On the other hand, resonant energy beams are more effective in damage to the tumor even at very low nanoagent concentrations.

The present simulations indicate that the nanoparticles can be used as a diagnostic agent with irradiation at the resonant energies, owing to the high contrast obtained between the normal tissue and the tumor by the dose enhancement. In fact, the enhanced low-energy photon absorption in the tumor via high-Z nanoparticles would render more visibility of the tumor by X-ray imaging and hence simultaneously reduce the amount of radiation exposure in diagnostics. However, for more accurate predictions of electron and photon productions, particularly

through the Auger cascade process, at resonant energies of the nanoparticles, further adoption and modifications of Geant4 to incorporate the shell structure are in the plan.

The scheme modeled in this work relies on the use of high-*Z* nanoparticles with large resonant cross sections and electron vacancies in higher shells. In order to implement the scheme, in practice, it is necessary to use multiple, at least two, monoenergetic beams: one to continuously create vacancies in higher shells due to Auger cascades, and the other for resonant excitation. For example, the Kα transition in gold at 68 keV requires gold ion(s) with at least one vacancy in the L-shell. This can be achieved by another beam at 82 keV, just above the K-ionization edge. A natural extension to improve the present work is to consider the two (or more) beams incident simultaneously: one with an energy slightly above the K-edge so to produce electron vacancies as the atom(s) breaks up due to Auger cascades, and a second beam at resonant energy to trigger resonant absorption and localized energy deposition. The combined effect of both beams can enhance even further the dose delivered to the tumor.

Whereas we have referred only to nanoparticles in this paper, our simulations rest basically on the behavior of individual atoms. However, the efficiency of energy deposition for theranostics is expected to depend on the shape, volume, and delivery mechanisms of the nanomaterial to the cancerous tumor. As such, it would be useful to simulate and compare different formations in addition to nanoparticles, such as nanorods or nanowires. For example, it is known that the density of different embedded nanostructures and their formation is related to chemical potential and surface ratios of ZnO nanowires.[23] However, to our knowledge, such nanostructures have not been studied for high-*Z* elements of interest in our simulations, which rest on the requirement that the K-shell resonant and ionization energies be sufficiently high to enable deep penetration of X-rays into the body tissue.

Acknowledgment. This work was partially supported by a Large Interdisciplinary Grant award by the Office of Research, the College of Mathematical and Physical Sciences, and the Department of Astronomy at the Ohio State University. The computational work was carried out at the Ohio Supercomputer Center in Columbus, Ohio.

References and Notes

(1) Pradhan, A. K.; Nahar, S. N.; Montenegro, M.; Yu, Y.; Zhang, H. L.; Sur, C.; Mrozik, M.; Pitzer, R. M. *J. Phys. Chem. A,* DOI: 10.1021/jp904977z.

(2) Silver, E.; Pradhan, A. K.; Yu, Y. *RT Image* **2008**, *21*, 30.

(3) Armen, G. B.; Aksela, H.; Abergand, T.; Aksela, S. *J. Phys. B* **2000**, *33*, R49.

(4) Takahashi, O.; Odelius, M.; Nordlund, D.; Nilsson, A.; Bluhm, H.; Pettersson, L. G. M. *J. Chem. Phys.* **2006**, *24*, 064307.

(5) Nahar, S. N.; Pradhan, A. K.; Sur, C. *J. Quant. Spectrosc. Radiat. Transfer* **2008**, *109*, 1951–1959.

(6) http://en.wikipedia.org/wiki/Monte_Carlo_method_for_photon_transport.

(7) (a) Agostinelli, S.; et al. *Nucl. Instrum. Methods Phys. Res., Sect. A* **2003**, *506*, 250–303. (b) Allison, J.; et al. *IEEE Trans. Nucl. Sci.* **2006**, *53*, 270–278.

(8) Blanc, D.; Terrissol, M. *Radiat. Prot. Dosim.* **1985**, *13*, 387–393.

(9) (a) Nelson, W. R.; Hirayama, H.; Rogers, D. W. O. *The EGS4 code system*, 1985. (b) Kawrakow,; Rogers, D. W. O. *The EGSnrc code system: Monte Carlo simulation of electron and photon transport*, 2006. (c) Hirayama, H.; Namito, Y.; Bielajew, A. F.; Wilderman, S. J.; Nelson, W. R. The EGS5 code system, 2006.

(10) (a) Fassó, A. *The physics models of FLUKA: Status and recent developments*, 2003. (b) Ferrari, A.; Sala, P. R.; Fassó, A.; Ranft, J. *FLUKA: A multi-particle transport code*, 2005.

(11) (a) *MCNP—A general Monte Carlo N-particle transport code*, version 5, 2003. (b) Forster, R. A. *Nucl. Instrum. Methods Phys. Res., Sect. B* **2004**, *213*, 82. (c) Hendricks, J. S. *MCNPX 2.3.0 user's guide (unrestricted distribution version)*, 2002. (d) Hendricks, J. S. *MCNPX*, version 26c, 2006.

(12) Nikjoo, H.; Uehara, S.; Emfietzoglou, D.; Cucinotta, F. *Radiat. Meas.* **2006**, *41*, 1052–1074.

(13) (a) Stepanek, J. *Med. Phys.* **2000**, *27*, 1544–1554. (b) Karnas, S.; Moiseenko, V.; Yu, E.; Truong, P.; Battista, J. *Radiat. Environ. Biophys.* **2001**, *40*, 199–206. (c) Moiseenko, V.; Karnas, S.; Yu, E.; Battista, J. *Radiat. Prot. Dosim.* **2002**, *99*, 113–116. (d) Pignol, J.-P.; Rakovitch, E.; Beachey, D.; Le Sech, C. *Int. J. Radiat. Oncol., Biol., Phys.* **2003**, *55*, 1082–1091.

(14) (a) Chauvie, S.; Francis, Z.; Guatelli, S.; Incerti, S.; Mascialino, B.; Moretto, P.; Nieminen, P.; Pia, M. *IEEE Trans. Nucl. Sci.* **2007**, *54*, 2619–2628. (b) Guatelli, S.; Mantero, A.; Mascialino, B.; Nieminen, P.; Pia, M. *IEEE Trans. Nucl. Sci.* **2007**, *54*, 585–593.

(15) Ivanchenko, V. N. *Nucl. Instrum. Methods Phys. Res., Sect. A* **2004**, *525*, 402–405 (Proceedings of the International Conference on Imaging Techniques in Subatomic Physics, Astrophysics, Medicine, Biology and Industry).

(16) (a) Rodrigues, P.; Moura, R.; Ortigao, C.; Peralta, L.; Pia, M.; Trindade, A.; Varela, J. *IEEE Trans. Nucl. Sci.* **2004**, *51*, 1412–1419. (b) Incerti, S.; Barberet, P.; Villeneuve, R.; Aguer, P.; Gontier, E.; Michelet-Habchi, C.; Moretto, P.; Nguyen, D.; Pouthier, T.; Smith, R. *IEEE Trans. Nucl. Sci.* **2004**, *51*, 1395–1401.

(17) (a) Amako, K.; Guatelli, S.; Ivanchencko, V.; Maire, M.; Mascialino, B.; Murakami, K.; Pandola, L.; Parlati, S.; Pia, M.; Piergentili, M.; Sasaki, T.; Urban, L. *Nucl. Phys. B, Proc. Suppl.* **2006**, *150*, 44–49 (Proceedings of the ninth Topical Seminar on Innovative Particle and Radiation Detectors). (b) Guatelli, S.; Mantero, A.; Mascialino, B.; Pia, M.; Zampichelli, V. *IEEE Trans. Nucl. Sci.* **2007**, *54*, 594–603.

(18) Mello, R. S.; Callisen, H.; Winter, J.; Kagan, A. R.; Norman, A. *Med. Phys.* **1983**, *10*, 75–78.

(19) Solberg, T. D.; Iwamoto, K. S.; Norman, A. *Phys. Med. Biol.* **1992**, *37*, 439–443.

(20) Rose, J. H.; Norman, A.; Ingram, M.; Aoki, C.; Solberg, T.; Mesa, A. *Int. J. Radiat. Oncol., Biol., Phys.* **1999**, *45*, 1127–1132.

(21) Boudou, C.; Balosso, J.; Esteve, F.; Elleaume, H. *Phys. Med. Biol.* **2005**, *50*, 4841–4851.

(22) Prezado, Y.; Fois, G.; Edouard, M.; Nemoz, C.; Renier, M.; Requardt, H.; Esteve, F.; Adam, J. F.; Elleaume, H.; Bravin, A. *Med. Phys.* **2009**, *36*, 725–733.

(23) Zhou, H.; Li, Z. *Mater. Chem. Phys.* **2005**, *89*, 326–331.

JP905323Y